Taming Brillouin Optomechanics Using Supermode Microresonators

Min Wang,[1,3,*] Zhi-Gang Hu,[1,3,*] Chenghao Lao,[1,2] Yuanlei Wang,[1,2] Xing Jin,[2] Xin Zhou,[1,3] Yuechen Lei,[1,3] Ze Wang,[2] Wenjing Liu,[2,5] Qi-Fan Yang,[2,5,†] and Bei-Bei Li[1,4,‡]

[1]*Beijing National Laboratory for Condensed Matter Physics, Institute of Physics, Chinese Academy of Sciences, Beijing 100190, China*

[2]*State Key Laboratory for Artificial Microstructure and Mesoscopic Physics and Frontiers Science Center for Nano-optoelectronics, School of Physics, Peking University, Beijing 100871, China*

[3]*University of Chinese Academy of Sciences, Beijing 100049, China*

[4]*Songshan Lake Materials Laboratory, Dongguan 523808, Guangdong, China*

[5]*Collaborative Innovation Center of Extreme Optics, Shanxi University, Taiyuan 030006, China*

(Received 27 July 2023; revised 27 November 2023; accepted 26 February 2024; published 26 March 2024; corrected 22 April 2024)

Electrostrictive Brillouin scattering provides a ubiquitous mechanism to optically excite high-frequency (>10 GHz), bulk acoustic phonons that are robust to surface-induced losses. Resonantly enhancing such photon-phonon interactions in high-Q microresonators has spawned diverse applications spanning microwave to optical domains. However, tuning both the pump and scattered waves into resonance usually comes with the cost of photon confinement or modal overlap, leading to limited optomechanical coupling. Here, we introduce Bragg scattering to realize strong bulk optomechanical coupling in the same spatial modes of a micron-sized supermode microresonator. A single-photon optomechanical coupling rate up to 12.5 kHz is demonstrated, showing more than 10 times improvement than other devices. Low-threshold phonon lasing and optomechanical strong coupling are also observed for the 10.2-GHz mechanical mode. Our work establishes a compact and efficient paradigm to optically control bulk acoustic phonons, paving the way toward optomechanical coupling at the single-photon level and providing a powerful engine for large-scale integration of quantum networks in which quantum states are massively transferred and stored.

DOI: 10.1103/PhysRevX.14.011056 Subject Areas: Optics, Photonics, Quantum Physics

I. INTRODUCTION

An illuminated bulk solid resembles the simplest optomechanical system, in which photons are scattered by bulk acoustic phonons via a combination of electrostriction and photoelastic effect [1–3]. Unlike many designated optomechanical oscillators [4–13], bulk optomechanics does not rely on the tight confinement of phonons, making it immune to any surface imperfections. Additionally, the phonons involved in the backward Brillouin scattering process have frequencies over gigahertz, which can be tuned over a broad range by adjusting the wavelength of the optical field. Given the low thermal occupancy of high-frequency phonons, bulk optomechanics has been regarded as a promising candidate for economic quantum systems, thereby easing the requirements for cryogenic setups [14].

The development of high-Q microresonators [15–18] has enabled the application of electrostrictive Brillouin scattering in nanophotonics. For example, the Stokes scattering process creates highly coherent Brillouin lasers [17,19] or phonon lasers [18,20], which have been harnessed for microwave synthesis [21], optical gyroscopes [22,23], high-speed communications [24], and microcomb generation [25–27]. Besides, the annihilation of phonons in the anti-Stokes scattering process has been exploited for optomechanical cooling [28,29] and optical isolation [30,31]. These advances are driven by the enhanced photon-phonon interaction, which is quantified by the single-photon optomechanical coupling rate [32]:

$$g_0/2\pi = \frac{1}{2\pi}\sqrt{v_p v_s \frac{g_B \hbar \omega_p \gamma_m}{4V_{\text{eff}}}}. \tag{1}$$

Here, v_p and v_s are the group velocities of the pump and Stokes field, respectively, g_B represents the bulk Brillouin gain coefficient, $\omega_p/2\pi$ is the frequency of the pump field, and $\Gamma_m/2\pi$ is the damping rate of the mechanical mode [33].

*These authors contributed equally to this work.

†leonardoyoung@pku.edu.cn

‡libeibei@iphy.ac.cn

In addition to these constants, g_0 is also dependent on the optical effective modal volume (V_{eff}), which is expressed as

$$V_{\text{eff}} = \frac{\int |E_p|^2 dV \int |E_S|^2 dV}{\int |E_p|^2 |E_S|^2 dV}, \tag{2}$$

where E_p and E_S denote the electric field intensity of the pump and Stokes fields, respectively [34]. A tightly confined optical device supporting perfectly matched optical and mechanical modes, thus, becomes the most ideal platform to realize strong Brillouin optomechanical coupling.

The phase-matching condition of Brillouin optomechanics imposes stringent geometric requirements on the microresonator. In the case of backward Brillouin scattering, the angular frequency difference between the pump and scattered waves should match the mechanical frequency

$$\Omega_m \approx \frac{2n v_m \omega_p}{c}, \tag{3}$$

where n is the refractive index and v_m represents the sound velocity. Typically, this offset is around 10 GHz for silica [15,19] and 7 GHz for chalcogenide glasses [16,35] at 1550 nm. These two materials are widely used in the field of Brillouin optomechanics. Figure 1(a) illustrates several microresonator configurations to achieve simultaneous matching of the pump and scattered waves to the cavity modes. The most common approach is by precisely controlling the resonator size to align the resonator's one or multiple free spectral ranges (FSRs) to the mechanical frequency [15–17,19,21–23,36–40]. However, it requires millimeter-to-centimeter-scale microresonators, which are less efficient in achieving large g_0. Moreover, Brillouin scattering exhibits cascading effects that prohibit the realization of high-power lasers or optomechanical strong coupling [41], unless additional structures are introduced to modify its resonant characteristics [39,40]. Another approach is based on microresonators supporting many transverse modes, which have a chance to provide a pair of optical modes with frequencies and azimuthal numbers satisfying the energy and momentum conservation criteria [18,25,27,42–45]. Although this method can be implemented in smaller devices without cascading effects, the optomechanical coupling rate is limited by the reduced modal overlaps.

II. DEVICE

In this work, we propose and demonstrate a new type of Brillouin optomechanical microresonator which features very large Brillouin optomechanical coupling rates. It is based on whispering gallery mode (WGM) microresonators, which have degenerate clockwise (CW) and counterclockwise (CCW) propagating modes. As shown in Fig. 1(a), by applying a periodic modulation to the boundary in the form of $\alpha\cos(2m\phi)$ (with α and ϕ representing the modulation amplitude and azimuthal angle along the cavity boundary, respectively), strong coupling between the two modes with azimuthal mode number m can be induced through Bragg scattering. As a result, the CW and CCW traveling-wave modes are hybridized into two standing-wave supermodes with a frequency splitting twice the coupling rate (β) [46–49].

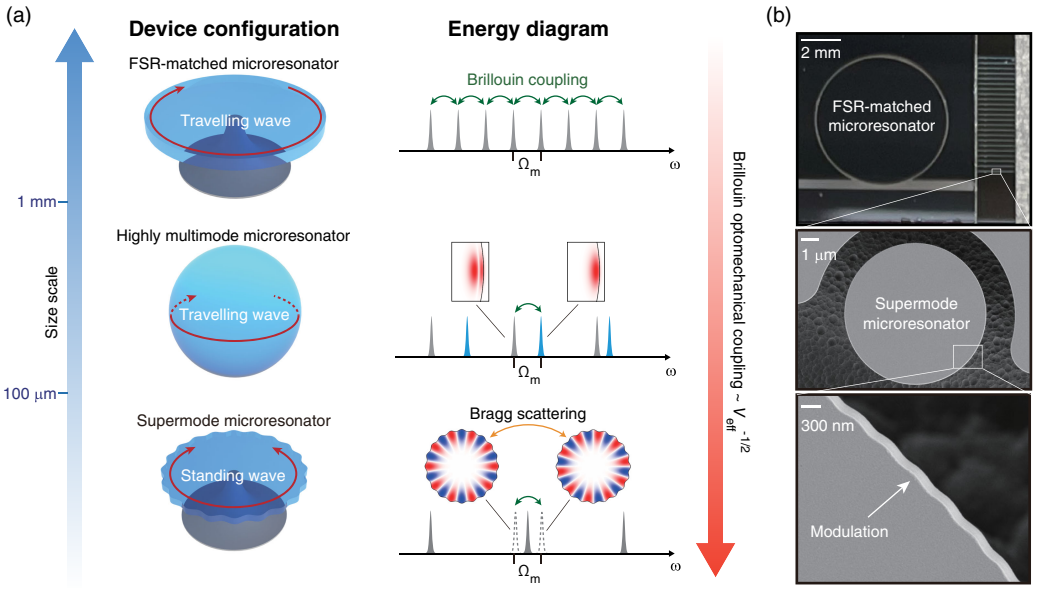

FIG. 1. Brillouin optomechanics in microresonators. (a) Microresonator configurations for efficient bulk Brillouin optomechanics. The resonant structures of the microresonators are plotted on the right. (b) Top: images showing FSR-matched microresonator (left) and supermode microresonators (right). Middle: scanning-electron-microscope image of the supermode microresonator. Bottom: enlarged view of the microresonator boundary.

One of the two supermodes has optical field maxima located at the modulation peaks, while the other mode has maxima at the modulation valleys. In contrast to randomized defects, this modulation impacts only the mode with azimuthal mode number m, thus leaving other modes unperturbed. Controlling the value of α allows for the frequency splitting to match the frequency of the bulk acoustic phonons, which enables efficient Brillouin optomechanical coupling in a much smaller footprint. As shown in Fig. 1(b), the footprint of the supermode microresonator is more than 4 orders of magnitude smaller than FSR-matched microresonators [15,16,19,21], despite that they are all made of silica with similar mechanical frequency.

We first determine the frequencies of the mechanical modes and their single-photon optomechanical coupling rates $g_0/2\pi$ by finite element method (FEM) simulation [50,51], with details presented in Appendix A and Sec. I in Supplemental Material [52]. Figure 2(a) presents the $g_0/2\pi$ for different mechanical modes for a microresonator with a radius of $r_0 = 20$ μm. The mechanical mode at 10.167 GHz has the largest $g_0/2\pi = 11.36$ kHz, with its strain distribution presented in the inset. The largest g_0 approximately scales with $V_{\text{eff}}^{-1/2}$ [32] as illustrated in Fig. S2 in Supplemental Material [52]. We then design the microresonators with frequency splittings between the two supermodes matching the frequencies of mechanical modes with the largest g_0. The relationship between frequency splitting and modulation amplitude is calculated for microresonators with radii of 15 and 20 μm, with the results presented in Fig. S3(a) in Supplemental Material [52].

To investigate the correlation between frequency splitting and modulation amplitude, we fabricate a series of SiO_2 microresonators utilizing the process outlined in Appendix B. As illustrated in Fig. S3(b) in Supplemental Material [52], we observe a monotonic increase in Δf with α, which approaches 10 GHz at $\alpha \sim 12$ nm. This value is in close proximity to the frequency of the mechanical mode (10.167 GHz) that produces the highest optomechanical coupling ($g_0/2\pi = 11.36$ kHz), as exhibited in Fig. 2(a). We then implement α in the range of 10–14 nm and $m = 101$ for microresonators with 20 μm radii [Figs. S3(a) and S3(b) [52]]. The transmission spectrum of the microresonator is obtained through a tapered fiber coupler, which clearly shows split resonances separated by 10.404 GHz at wavelengths near 1554 nm [Fig. 2(c)]. Fitting the resonances using Lorentzian line shape yields intrinsic decay rates $\kappa_0/2\pi$ of 85 MHz, which suggests that the Q factor exceeds 2 million.

III. PHONON LASING

Using the experimental setup shown in Fig. S9(a) in Supplemental Material [52], we pump the higher-frequency split mode in the CW direction to amplify the Stokes photons and mechanical phonons. Since the damping rate of the phonons (around 60 MHz) is smaller than that of the photons (around 100 MHz), the Brillouin gain rises to

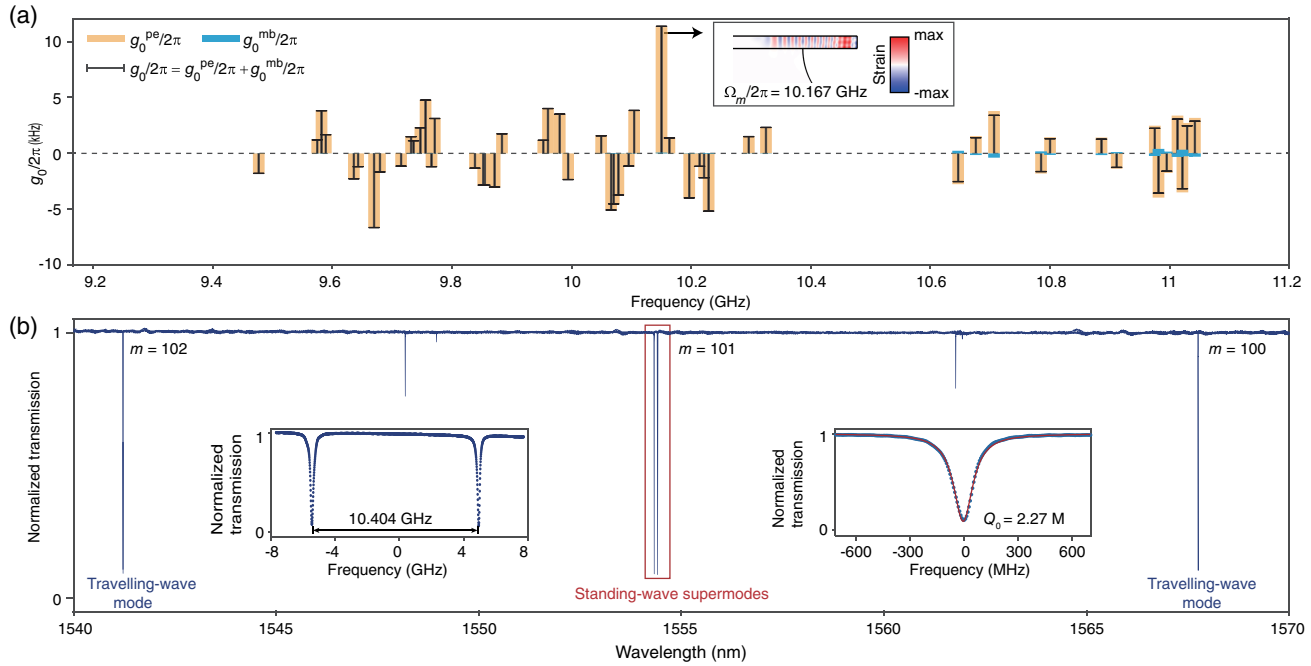

FIG. 2. Supermode microresonator. (a) Simulated single-photon optomechanical coupling rate ($g_0/2\pi$) of different mechanical modes in a microresonator with 20 μm radius. The contributions from the photoelastic effect ($g_0^{pe}/2\pi$, orange columns) and the moving boundary effect ($g_0^{mb}/2\pi$, blue columns) are both indicated. (b) Transmission spectrum of a SiO_2 microresonator with $r_0 = 20$ μm and $\alpha \approx 12.6$ nm, where the target mode has an azimuthal mode number of $m = 101$. Insets provide enlarged views of the frequency splitting and Q factor.

compensate for the propagation losses of phonons and lead to phonon lasing actions [18,53]. The power of the Stokes photons in both CW and CCW directions are simultaneously monitored by two optical spectral analyzers (OSAs) [Fig. 3(b)]. Once the pump power exceeds the lasing threshold, an appreciable amount of Stokes photons are observed in both directions with approximately equal power due to the strong backscattering [Fig. 3(c)]. The lasing threshold is determined to be around 8.28 mW.

The linewidth of the phonon laser $\Delta\nu_m$ has two origins [53], one from thermal noise (known as the Schawlow-Townes linewidth $\Delta\nu_m^{\mathrm{th}}$) and the other induced by pump noise ($\Delta\nu_m^{p}$). The former is inversely proportional to the intracavity phonon number [$\Delta\nu_m^{\mathrm{th}} = \gamma_m n_{\mathrm{th}}/(4\pi N)$], where, for room temperature, $n_{\mathrm{th}} \sim 610$ is the average thermal occupancy of Brillouin phonons and N denotes the intracavity Brillouin phonon number. The latter, on the other hand, is a constant value $\Delta\nu_m^{p} = \Delta\nu_p/[(1+\kappa/\gamma_m)^2]$, where $\Delta\nu_p$ is the linewidth of the pump laser. In our experiment, we utilize the multispectral delayed self-heterodyne technique [54–57] to measure the linewidth of the phonon laser (see Appendix C and Sec. IV in Supplemental Material [52]). The instantaneous phases of the pump and Stokes lasers are measured, and the difference in these values provides the phase evolution as well as the frequency noise of the phonon laser. The frequency noise power spectral densities of the phonon laser at four different power levels (corresponding to four different phonon numbers N) are plotted in Fig. 3(d). The linewidth of the phonon laser is inferred from the white noise at frequency offsets between 100 kHz and 2 MHz. Our results show that the phonon linewidth is inversely proportional to the power of the Stokes laser, decreasing from 1.5 kHz at 0.1 mW to 68.8 Hz at 5 mW [Fig. 3(e)]. The frequency of the phonon laser is also obtained from the beat note between the pump and Stokes lasers as 10.3 GHz. It differs slightly from the expected frequency of the mechanical mode at 10.167 GHz, which is suspected due to the frequency-pulling effect [19].

IV. STRONG COUPLING

We pump the lower-frequency split mode with the purpose of realizing optomechanical strong coupling between the photons and the bulk acoustic phonons. As shown in Fig. 4(a), this generates an anti-Stokes field while satisfying momentum and energy conservation. Once the coupling rate $G > \sqrt{(\kappa^2+\gamma_m^2)/8}$ (see Sec. V in

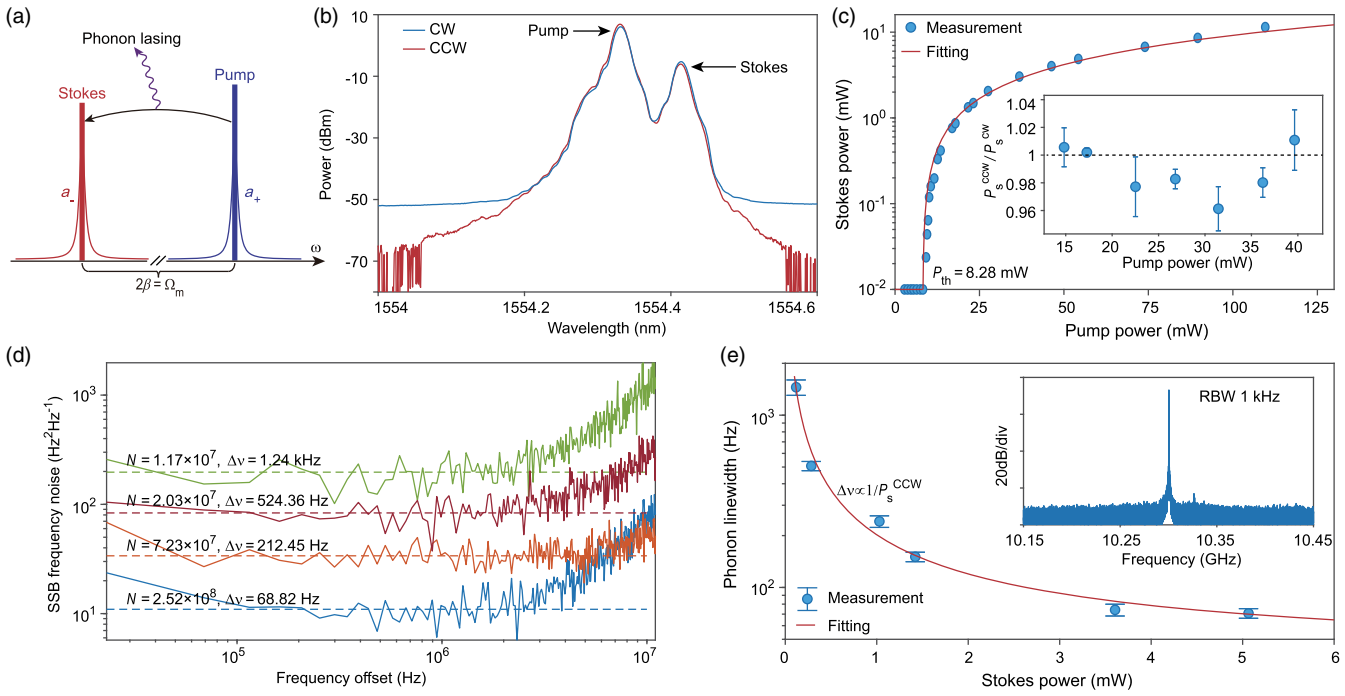

FIG. 3. Observation of phonon lasing. (a) Schematics of the physical mechanisms of phonon lasing when pumping at the higher-frequency split mode. (b) Optical spectra of stimulated Brillouin scattering (SBS) in both the CW and CCW directions when the pump light is coupled into the higher-frequency split mode in the CW direction. (c) Stokes power in the CW direction (P_S^{CW}) as a function of the pump power, revealing a threshold power of $P_{\mathrm{th}} \approx 8.28$ mW. Inset: the ratio of the Stokes powers in the CCW and CW directions, which maintains approximately 1. (d) Single-sideband (SSB) frequency noise spectra of phonon lasers with different Stokes powers coupled out of the microresonator. The green, red, orange, and blue curves correspond to the coupled out Stokes power in the CW direction (P_S^{CW}) of 0.167, 0.289, 1.03, and 3.59 mW, respectively. (e) Phonon linewidth as a function of the coupled out Stokes power in the CCW direction. Inset: electronic spectrum displaying the mechanical frequency at 10.3 GHz.

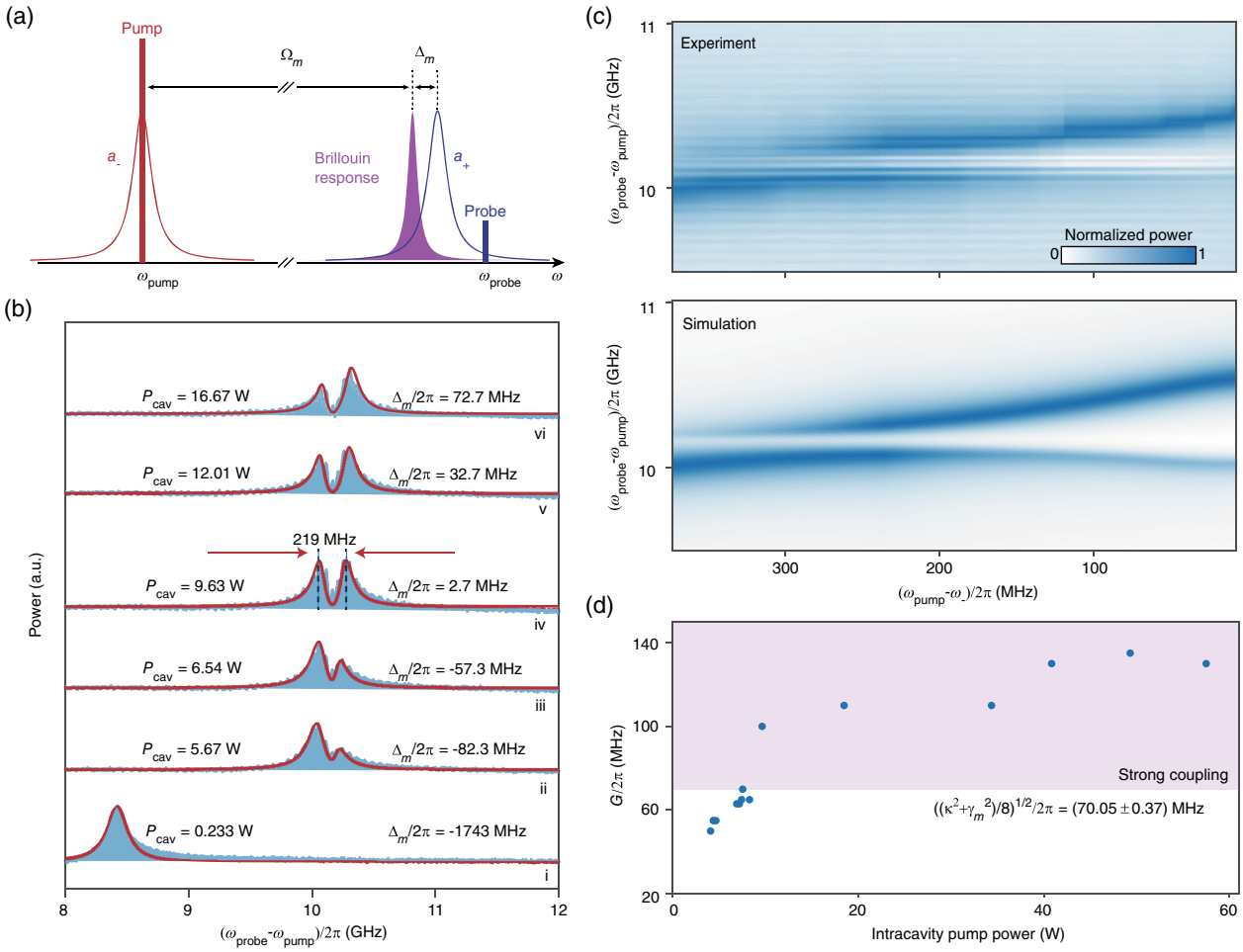

FIG. 4. Observation of optomechanical strong coupling. (a) Schematic illustrating the resonance structure for the anti-Stokes process. A pump laser with frequency ω_{pump} drives the lower-frequency split mode a_-. The higher-frequency sideband of the pump laser, generated by the EOM at a frequency of ω_{probe}, is used to probe the higher-frequency split mode a_+. The frequency separation between a_+ mode and the Brillouin gain peak is denoted as $\Delta_m = \omega_+ - \omega_{\mathrm{pump}} - \Omega_m$. (b) Power spectra around the high-frequency split mode. As the detuning $\omega_{\mathrm{pump}} - \omega_-$ decreases from bottom to top, the intracavity pump power (P_{cav}) increases, and the frequency difference between two photonic-phononic hybrid modes first decreases and then increases, showing a trend of avoided mode crossing. (c) Comparison of experimentally measured (top) and theoretically predicted (bottom) spectra as a function of the frequency detuning $\omega_{\mathrm{pump}} - \omega_-$. (d) Optomechanical coupling rate ($G/2\pi$) derived from the measured spectra, plotted as a function of the intracavity pump power (P_{cav}).

Supplemental Material [52]), a strong coupling regime emerges, causing the hybridization of initial optical and mechanical modes into two photonic-phononic hybrid modes. Such an optomechanical strong coupling phenomenon can be interrogated through heterodyne detection (see Appendix C and Fig. S11 [52]). The pump laser with frequency ω_{pump} and detuning $\omega_{\mathrm{pump}} - \omega_-$ is injected into the microresonator in the CW direction. The probe laser is created by phase modulating the pump laser using a vector network analyzer. Scanning the frequency of the driving microwave signals reveals the eigenstates at the a_+ frequency. Plotted in Fig. 4(b) are the results obtained at different stages when the pump laser is tuned into the resonance. This effectively changes the intracavity pump power in the microresonator P_{cav}. At low power levels, only one peak is observed near the a_+ wavelength. Increasing the intracavity pump power leads to two distinct and well-resolved peaks, highlighting the presence of in-phase and out-of-phase hybrid photonic-phononic modes. When the intensity of these two peaks is approximately equal at stage (iv) corresponding to $\Delta_m/2\pi = 2.7$ MHz, the frequency splitting between them is approximately 219 MHz, which exceeds their respective linewidths. Fitting the spectra based on experimental parameters ($\kappa/2\pi = 190$ MHz and $\Omega_m/2\pi = 10.167$ GHz) reveals the damping rate of the mechanical mode to be $\gamma_m/2\pi = (60.43 \pm 8.09)$ MHz and $G/2\pi = 100$ MHz at stage (iv). Additionally, we estimate the single-photon optomechanical coupling rate to be $g_0/2\pi = (12.52 \pm 2.33)$ kHz, which exceeds that of the previous work [45] by a factor of 30.

TABLE I. Summary of experimental parameters for various Brillouin optomechanical resonator systems that are dominated by the photoelastic effect. ⋯ indicates that the data are not available.

Material	Structure	$\Omega_m/2\pi$ (GHz)	Footprint (mm^2)	g_B (mm/GW)	$g_0/2\pi$ (kHz)	$C_0 = (4g_0^2/\kappa\gamma_m)$	Refs.
SiO_2	Disk	10.898	28.46	45	0.68[a]	2.803×10^{-8}	[15,19]
As_2S_3	Ring	7.6	0.4	715	12.14[a]	3.05×10^{-8}	[16]
Si_3N_4	Ring	10.93	437.42	45	0.2[a]	1.67×10^{-10}	[17]
Si	Racetrack	6.02	12.57	~70	1.76	1.1×10^{-8}	[18]
SiO_2	Sphere	11.5	3.14×10^{-2}	45	⋯	⋯	[42]
CaF_2	Rod	17.5	23.93	28	0.06[a]	4.5×10^{-10}	[36]
SiO_2	Sphere	0.095[b]	1.89×10^{-2}	45	0.02	1.074×10^{-7}	[29]
SiO_2	Rod	11.0	0.39	45	0.4	2.5×10^{-9}	[45]
SiO_2	Disk	10.167	1.26×10^{-3}	45	12.52	1.015×10^{-7}	This work

[a]The value shown is calculated through the related parameters according to Eq. (1).
[b]The mechanical frequency in this work is significantly lower compared to other silica microresonaters, as it is forward Brillouin scattering in this case.

Figure 4(c) demonstrates excellent agreement between measured and theoretically predicted evolution of the eigenstates as a function of pump-cavity detuning. The spectra exhibit an unambiguous avoided mode crossing, providing clear evidence of optomechanical strong coupling. Figure 4(d) illustrates the measured optomechanical coupling rate as a function of intracavity pump power. The system attains strong coupling when the intracavity pump power exceeds 7.54 W. It is worth noting that most third-order nonlinear processes, e.g., stimulated Raman scattering and four-wave mixing, are not observed in the experiment, due to the much higher thresholds. We observe third-harmonic generation only when the pump power is increased to around 800 mW, since it does not require a threshold power to initiate (see Fig. S10 in Sec. IV in Supplemental Material [52]).

V. DISCUSSION

Table I and Fig. 5(a) summarize the values of g_0 reported in various Brillouin optomechanical platforms primarily driven by electrostrictive and photoelastic effects. Notably, our device exhibits the highest $g_0/2\pi = 12.52$ kHz, which is 18 times larger than the best results demonstrated in silica microresonators [15,17,19]. Even when compared with As_2S_3 microresonators, which have a 16 times larger Brillouin gain coefficient [16], our device still demonstrates a competitive g_0. This highlights the importance of achieving both a small modal volume and perfect modal overlap. We also calculate the single-photon cooperativity $C_0 = (4g_0^2)/(\kappa\gamma_m)$ for these platforms to evaluate their potential in quantum manipulation. Once again, our device stands out with the largest C_0 due to its significantly higher g_0, as shown in Fig. 5(b). In addition, the optical Q factor reported in this work is the highest among all supermode microresonators using engraved nanometric gratings [58–64].

Currently, the linewidth of the optical modes is larger than that of the mechanical modes, resulting in phonon lasing action instead of photon lasing. However, the achieved Q factor is still far below the Bragg-grating-induced scatting loss limited Q factor, which is higher than the level of 10^8. Further improvement of the Q factor would enable high-density integration of compact Brillouin lasers. The terminated cascading process also benefits the output

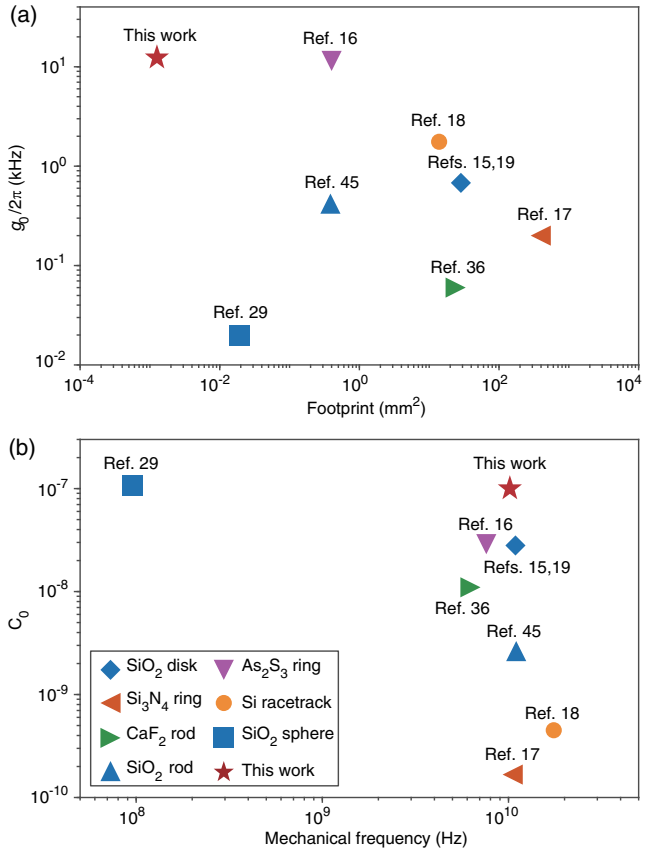

FIG. 5. Comparison of optomechanical microresonators driven by photoelastic effect. (a) Single-photon optomechanical coupling rate $g_0/2\pi$ versus the footprint of the resonator. (b) Single-photon cooperativity C_0 versus the mechanical frequency.

power and coherence [19]. Additionally, the bidirectional emission of the Brillouin laser would simplify photonic integration by eliminating the need for difficult-to-integrate optical circulators.

Finally, it is important to note that the supermode microresonator configuration is compatible with any material platform. For instance, changing the material from silica to chalcogenide glass could result in a 10 times stronger g_0, due to the larger Brillouin gain coefficient [16,35] and the smaller modal volume it can achieve. It, thus, holds great potential for ground-state cooling and coherent quantum manipulation of bulk acoustic phonons, especially when their lifetimes are remarkably extended at cryogenic temperatures [14].

ACKNOWLEDGMENTS

The authors thank Yun-Feng Xiao, Jun-Qiu Liu, and Xiao-Chong Yu for helpful discussions and the funding support from the National Key Research and Development Program of China (2021YFA1400700), the National Natural Science Foundation of China (NSFC) (62222515, 12174438, 11934019, 91950118, and 92150108), the basic frontier science research program of Chinese Academy of Sciences (ZDBS-LY-JSC003), Beijing Natural Science Foundation (Z210004), and CAS Project for Young Scientists in Basic Research (YSBR-100). The fabrication in this work is supported by the Micro/nano Fabrication Laboratory of Synergetic Extreme Condition User Facility (SECUF) and the Advanced Photonics Integrated Center of Peking University.

APPENDIX A: SIMULATION OF SINGLE-PHOTON OPTOMECHANICAL COUPLING RATES

To design the SiO_2 microresonators with suitable mode splittings, we perform FEM simulations using COMSOL MULTIPHYSICS to obtain the field distributions of the optical and mechanical modes (Fig. S1 in Supplemental Material [52]). In the simulations, we employ the following parameters for the microresonator with a radius of $r_0 = 20$ μm. The azimuthal mode numbers for the pump, Stokes, and mechanical modes are 101, −101, and 202, respectively. The refractive index of SiO_2 is $n = 1.446$, while the density, Young's modulus, and Poisson's ratio are $\rho_{SiO_2} = 2260\ \mathrm{kg/m^3}$, $E_{SiO_2} = 73.1$ GPa, and $\nu = 0.17$, respectively. The single-photon optomechanical coupling rate can be calculated using the method introduced in Refs. [50,51] (details in Sec. I in Supplemental Material [52]), which relies on the spatial overlap between the mechanical and optical modes. The g_0 comprises two components, one resulting from the photoelastic effect (g_0^{pe}) and the other from the moving boundary effect (g_0^{mb}), with their sum yielding the total g_0, i.e., $g_0 = g_0^{\mathrm{pe}} + g_0^{\mathrm{mb}}$.

APPENDIX B: DEVICE FABRICATION

The devices are fabricated on 1-μm-thick thermal oxide on silicon chips. Microresonator patterns are defined using AR-P-6200 resist by electron-beam lithography with an acceleration voltage of 125 kV and a current of 500 pA. In addition, two 13-μm-long and 1-μm-wide microbridges are patterned on both sides of the resonator to ensure stable tapered fiber coupling, albeit at a cost of 10% optical loss per direction. Transferring the etching mask to the oxide layer is achieved via a combination of dry etching techniques, starting with an inductively coupled plasma etching utilizing a C_4F_8/Ar chemistry to etch approximately 900 nm thickness of SiO_2, followed by a reactive ion etching with a CHF_3/Ar chemistry to etch the remaining SiO_2. Following the etching process, standard cleaning techniques are employed to remove the resist and organic materials. Finally, the silicon is isotropically etched using xenon difluoride, creating an air-cladding WGM microresonator. To suppress the mechanical oscillation of the microdisk, particularly the low-frequency mechanical modes at the megahertz level such as the radial breathing mode and flapping mode, the amount of undercut during silicon etching is set to approximately 5 μm.

APPENDIX C: DETAILED EXPERIMENTAL SETUP

The experimental setup for phonon lasing and measurement is presented in Fig. S9 in Supplemental Material [52]. A tunable continuous-wave (cw) laser is amplified using an erbium-doped fiber amplifier and then coupled into the SiO_2 microresonator via a tapered fiber. The transmitted light from the SiO_2 microresonator, including both the pump and Stokes light, is split into three channels. The first channel is detected by a photodetector, and the transmission spectrum of the SiO_2 microresonator is measured by an oscilloscope. The second channel is detected by another photodetector and measured by an electronic spectrum analyzer to obtain the phonon laser spectrum. The third channel is directed to an OSA to obtain the SBS spectrum. Starting from the blue-detuned side of the higher-frequency split mode, the wavelength of the pump laser is gradually scanned up. The phonon laser linewidth is measured by analyzing the backscattered pump and Stokes light from the SiO_2 microresonator. Additional details on the linewidth measurement technique can be found in Sec. IV in Supplemental Material [52].

The experimental setup for measuring the optomechanical strong coupling is illustrated in Fig. S13 in Supplemental Material [52]. A cw laser is used to pump the lower-frequency split mode, and its frequency ω_{pump} is thermally locked to the cavity resonance with a detuning of $\omega_{\mathrm{pump}} - \omega_{-}$. The transmission spectrum around the pump mode of the SiO_2 microresonator is detected by a photodetector and monitored by an oscilloscope, while the

reflected light from the SiO_2 microresonator is detected by another photodetector. An electro-optic modulator (EOM) is employed to modulate the pump light, with its modulation frequency being scanned using a vector network analyzer (VNA). When the probe light is resonant with the higher-frequency split mode a_+, both the pump and probe light can couple into and out of the SiO_2 microresonator, generating a beat note signal at a frequency of $\omega_{\text{probe}} - \omega_{\text{pump}}$ that can be measured in the optical response spectrum S_{21} by the VNA.

[1] R. Boyd, *Nonlinear Optics*, 3rd ed. (Academic, Burlington, 2008).

[2] B. J. Eggleton, C. G. Poulton, and R. Pant, *Inducing and harnessing stimulated Brillouin scattering in photonic integrated circuits*, Adv. Opt. Photonics **5**, 536 (2013).

[3] M. Merklein, I. V. Kabakova, T. F. Büttner, D.-Y. Choi, B. Luther-Davies, S. J. Madden, and B. J. Eggleton, *Enhancing and inhibiting stimulated Brillouin scattering in photonic integrated circuits*, Nat. Commun. **6**, 6396 (2015).

[4] C. Dong, V. Fiore, M. C. Kuzyk, and H. Wang, *Optomechanical dark mode*, Science **338**, 1609 (2012).

[5] B.-B. Li, J. Bilek, U. B. Hoff, L. S. Madsen, S. Forstner, V. Prakash, C. Schäfermeier, T. Gehring, W. P. Bowen, and U. L. Andersen, *Quantum enhanced optomechanical magnetometry*, Optica **5**, 850 (2018).

[6] T. Kippenberg, H. Rokhsari, T. Carmon, A. Scherer, and K. Vahala, *Analysis of radiation-pressure induced mechanical oscillation of an optical microcavity*, Phys. Rev. Lett. **95**, 033901 (2005).

[7] S. Basiri-Esfahani, A. Armin, S. Forstner, and W. P. Bowen, *Precision ultrasound sensing on a chip*, Nat. Commun. **10**, 123 (2019).

[8] J. Rosenberg, Q. Lin, and O. Painter, *Static and dynamic wavelength routing via the gradient optical force*, Nat. Photonics **3**, 478 (2009).

[9] Q. Lin, J. Rosenberg, D. Chang, R. Camacho, M. Eichenfield, K. J. Vahala, and O. Painter, *Coherent mixing of mechanical excitations in nano-optomechanical structures*, Nat. Photonics **4**, 236 (2010).

[10] E. Gavartin, P. Verlot, and T. J. Kippenberg, *A hybrid on-chip optomechanical transducer for ultrasensitive force measurements*, Nat. Nanotechnol. **7**, 509 (2012).

[11] J. Chan, T. Alegre, A. H. Safavi-Naeini, J. T. Hill, A. Krause, S. Gröblacher, M. Aspelmeyer, and O. Painter, *Laser cooling of a nanomechanical oscillator into its quantum ground state*, Nature (London) **478**, 89 (2011).

[12] W. Jiang, C. J. Sarabalis, Y. D. Dahmani, R. N. Patel, F. M. Mayor, T. P. McKenna, R. Van Laer, and A. H. Safavi-Naeini, *Efficient bidirectional piezo-optomechanical transduction between microwave and optical frequency*, Nat. Commun. **11**, 1166 (2020).

[13] S. Hönl, Y. Popoff, D. Caimi, A. Beccari, T. J. Kippenberg, and P. Seidler, *Microwave-to-optical conversion with a gallium phosphide photonic crystal cavity*, Nat. Commun. **13**, 2065 (2022).

[14] W. Renninger, P. Kharel, R. Behunin, and P. Rakich, *Bulk crystalline optomechanics*, Nat. Phys. **14**, 601 (2018).

[15] H. Lee, T. Chen, J. Li, K. Y. Yang, S. Jeon, O. Painter, and K. J. Vahala, *Chemically etched ultrahigh-Q wedge-resonator on a silicon chip*, Nat. Photonics **6**, 369 (2012).

[16] B. Morrison, A. Casas-Bedoya, G. Ren, K. Vu, Y. Liu, A. Zarifi, T. G. Nguyen, D.-Y. Choi, D. Marpaung, S. J. Madden *et al.*, *Compact Brillouin devices through hybrid integration on silicon*, Optica **4**, 847 (2017).

[17] S. Gundavarapu, G. M. Brodnik, M. Puckett, T. Huffman, D. Bose, R. Behunin, J. Wu, T. Qiu, C. Pinho, N. Chauhan *et al.*, *Sub-hertz fundamental linewidth photonic integrated Brillouin laser*, Nat. Photonics **13**, 60 (2019).

[18] N. T. Otterstrom, R. O. Behunin, E. A. Kittlaus, Z. Wang, and P. T. Rakich, *A silicon Brillouin laser*, Science **360**, 1113 (2018).

[19] J. Li, H. Lee, T. Chen, and K. J. Vahala, *Characterization of a high coherence, Brillouin microcavity laser on silicon*, Opt. Express **20**, 20170 (2012).

[20] X. He, G. I. Harris, C. G. Baker, A. Sawadsky, Y. L. Sfendla, Y. P. Sachkou, S. Forstner, and W. P. Bowen, *Strong optical coupling through superfluid Brillouin lasing*, Nat. Phys. **16**, 417 (2020).

[21] J. Li, H. Lee, and K. J. Vahala, *Microwave synthesizer using an on-chip Brillouin oscillator*, Nat. Commun. **4**, 1 (2013).

[22] J. Li, M.-G. Suh, and K. Vahala, *Microresonator Brillouin gyroscope*, Optica **4**, 346 (2017).

[23] Y.-H. Lai, M.-G. Suh, Y.-K. Lu, B. Shen, Q.-F. Yang, H. Wang, J. Li, S. H. Lee, K. Y. Yang, and K. Vahala, *Earth rotation measured by a chip-scale ring laser gyroscope*, Nat. Photonics **14**, 345 (2020).

[24] G. M. Brodnik, M. W. Harrington, J. H. Dallyn, D. Bose, W. Zhang, L. Stern, P. A. Morton, R. O. Behunin, S. B. Papp, and D. J. Blumenthal, *Optically synchronized fibre links using spectrally pure chip-scale lasers*, Nat. Photonics **15**, 588 (2021).

[25] Y. Bai, M. Zhang, Q. Shi, S. Ding, Y. Qin, Z. Xie, X. Jiang, and M. Xiao, *Brillouin-Kerr soliton frequency combs in an optical microresonator*, Phys. Rev. Lett. **126**, 063901 (2021).

[26] I. H. Do, D. Kim, D. Jeong, D. Suk, D. Kwon, J. Kim, J. H. Lee, and H. Lee, *Self-stabilized soliton generation in a microresonator through mode-pulled Brillouin lasing*, Opt. Lett. **46**, 1772 (2021).

[27] H. Zhang, T. Tan, H.-J. Chen, Y. Yu, W. Wang, B. Chang, Y. Liang, Y. Guo, H. Zhou, H. Xia *et al.*, *Soliton microcombs multiplexing using intracavity-stimulated Brillouin lasers*, Phys. Rev. Lett. **130**, 153802 (2023).

[28] M. Tomes, F. Marquardt, G. Bahl, and T. Carmon, *Quantum-mechanical theory of optomechanical Brillouin cooling*, Phys. Rev. A **84**, 063806 (2011).

[29] G. Bahl, M. Tomes, F. Marquardt, and T. Carmon, *Observation of spontaneous Brillouin cooling*, Nat. Phys. **8**, 203 (2012).

[30] C.-H. Dong, Z. Shen, C.-L. Zou, Y.-L. Zhang, W. Fu, and G.-C. Guo, *Brillouin-scattering-induced transparency and non-reciprocal light storage*, Nat. Commun. **6**, 6193 (2015).

[31] J. Kim, M. C. Kuzyk, K. Han, H. Wang, and G. Bahl, *Non-reciprocal Brillouin scattering induced transparency*, Nat. Phys. **11**, 275 (2015).

[32] R. Van Laer, R. Baets, and D. Van Thourhout, *Unifying Brillouin scattering and cavity optomechanics*, Phys. Rev. A **93**, 053828 (2016).

[33] Govind Agrawal, *Nonlinear Fiber Optics*, 5th ed. (Academic, New York, 2013), Chap. 9.
[34] T. J. Kippenberg, S. M. Spillane, B. Min, and K. J. Vahala, *Theoretical and experimental study of stimulated and cascaded Raman scattering in ultrahigh-Q optical microcavities*, IEEE J. Sel. Top. Quantum Electron. **10**, 1219 (2004).
[35] R. Pant, C. G. Poulton, D.-Y. Choi, H. Mcfarlane, S. Hile, E. Li, L. Thevenaz, B. Luther-Davies, S. J. Madden, and B. J. Eggleton, *On-chip stimulated Brillouin scattering*, Opt. Express **19**, 8285 (2011).
[36] I. S. Grudinin, A. B. Matsko, and L. Maleki, *Brillouin lasing with a* CaF_2 *whispering gallery mode resonator*, Phys. Rev. Lett. **102**, 043902 (2009).
[37] K. Y. Yang, D. Y. Oh, S. H. Lee, Q.-F. Yang, X. Yi, B. Shen, H. Wang, and K. Vahala, *Bridging ultrahigh-Q devices and photonic circuits*, Nat. Photonics **12**, 297 (2018).
[38] N. Chauhan, A. Isichenko, K. Liu, J. Wang, Q. Zhao, R. O. Behunin, P. T. Rakich, A. M. Jayich, C. Fertig, C. Hoyt *et al.*, *Visible light photonic integrated Brillouin laser*, Nat. Commun. **12**, 4685 (2021).
[39] M. Puckett, D. Bose, K. Nelson, and D. J. Blumenthal, *Higher order cascaded SBS suppression using gratings in a photonic integrated ring resonator laser*, in *CLEO: Science and Innovations* (Optica Publishing Group, Washington, DC, 2019), pp. SM4O-1.
[40] K. Liu, J. Wang, N. Chauhan, M. W. Harrington, K. D. Nelson, and D. J. Blumenthal, *Integrated photonic molecule Brillouin laser with high power sub-100-mHz fundamental linewidth*, Opt. Lett. **49**, 45 (2024).
[41] R. O. Behunin, N. T. Otterstrom, P. T. Rakich, S. Gundavarapu, and D. J. Blumenthal, *Fundamental noise dynamics in cascaded-order Brillouin lasers*, Phys. Rev. A **98**, 023832 (2018).
[42] M. Tomes and T. Carmon, *Photonic micro-electromechanical systems vibrating at X-band (11-GHz) rates*, Phys. Rev. Lett. **102**, 113601 (2009).
[43] G. Bahl, J. Zehnpfennig, M. Tomes, and T. Carmon, *Stimulated optomechanical excitation of surface acoustic waves in a microdevice*, Nat. Commun. **2**, 1 (2011).
[44] C. Guo, K. Che, Z. Cai, S. Liu, G. Gu, C. Chu, P. Zhang, H. Fu, Z. Luo, and H. Xu, *Ultralow-threshold cascaded Brillouin microlaser for tunable microwave generation*, Opt. Lett. **40**, 4971 (2015).
[45] G. Enzian, M. Szczykulska, J. Silver, L. Del Bino, S. Zhang, I. A. Walmsley, P. Del'Haye, and M. R. Vanner, *Observation of Brillouin optomechanical strong coupling with an 11 GHz mechanical mode*, Optica **6**, 7 (2019).
[46] A. Mazzei, S. Götzinger, L. d. S. Menezes, G. Zumofen, O. Benson, and V. Sandoghdar, *Controlled coupling of counterpropagating whispering-gallery modes by a single rayleigh scatterer: a classical problem in a quantum optical light*, Phys. Rev. Lett. **99**, 173603 (2007).
[47] J. Zhu, S. K. Ozdemir, Y.-F. Xiao, L. Li, L. He, D.-R. Chen, and L. Yang, *On-chip single nanoparticle detection and sizing by mode splitting in an ultrahigh-Q microresonator*, Nat. Photonics **4**, 46 (2010).
[48] B.-B. Li, W. R. Clements, X.-C. Yu, K. Shi, Q. Gong, and Y.-F. Xiao, *Single nanoparticle detection using split-mode microcavity Raman lasers*, Proc. Natl. Acad. Sci. U.S.A. **111**, 14657 (2014).
[49] P.-J. Zhang, Q.-X. Ji, Q.-T. Cao, H. Wang, W. Liu, Q. Gong, and Y.-F. Xiao, *Single-mode characteristic of a supermode microcavity Raman laser*, Proc. Natl. Acad. Sci. U.S.A. **118**, e2101605118 (2021).
[50] G. S. Wiederhecker, P. Dainese, and T. P. Mayer Alegre, *Brillouin optomechanics in nanophotonic structures*, APL Photonics **4**, 071101 (2019).
[51] Y. A. Espinel, F. G. Santos, G. O. Luiz, T. M. Alegre, and G. S. Wiederhecker, *Brillouin optomechanics in coupled silicon microcavities*, Sci. Rep. **7**, 43423 (2017).
[52] See Supplemental Material at http://link.aps.org/supplemental/10.1103/PhysRevX.14.011056 for the simulation details of single-photon optomechanical coupling rate, theoretical studies and experimental details on phonon lasing and strong coupling.
[53] J. Xiong, Z. Huang, K. Cui, X. Feng, F. Liu, W. Zhang, and Y. Huang, *Phonon and photon lasing dynamics in optomechanical cavities*, Fundam. Res. **3**, 37 (2023).
[54] D. Jeong, D. Kwon, I. Jeon, I. H. Do, J. Kim, and H. Lee, *Ultralow jitter silica microcomb*, Optica **7**, 1108 (2020).
[55] T. Tetsumoto, T. Nagatsuma, M. E. Fermann, G. Navickaite, M. Geiselmann, and A. Rolland, *Optically referenced 300 GHz millimetre-wave oscillator*, Nat. Photonics **15**, 516 (2021).
[56] Z. Yuan, H. Wang, P. Liu, B. Li, B. Shen, M. Gao, L. Chang, W. Jin, A. Feshali, M. Paniccia *et al.*, *Correlated self-heterodyne method for ultra-low-noise laser linewidth measurements*, Opt. Express **30**, 25147 (2022).
[57] C. Lao, X. Jin, L. Chang, H. Wang, Z. Lv, W. Xie, H. Shu, X. Wang, J. E. Bowers, and Q.-F. Yang, *Quantum decoherence of dark pulses in optical microresonators*, Nat. Commun. **14**, 1802 (2023).
[58] X. Lu, S. Rogers, W. C. Jiang, and Q. Lin, *Selective engineering of cavity resonance for frequency matching in optical parametric processes*, Appl. Phys. Lett. **105**, 151104 (2014).
[59] S.-P. Yu, D. C. Cole, H. Jung, G. T. Moille, K. Srinivasan, and S. B. Papp, *Spontaneous pulse formation in edgeless photonic crystal resonators*, Nat. Photonics **15**, 461 (2021).
[60] S.-P. Yu, E. Lucas, J. Zang, and S. B. Papp, *A continuum of bright and dark-pulse states in a photonic-crystal resonator*, Nat. Commun. **13**, 3134 (2022).
[61] X. Lu, A. Rao, G. Moille, D. A. Westly, and K. Srinivasan, *Universal frequency engineering tool for microcavity nonlinear optics: Multiple selective mode splitting of whispering-gallery resonances*, Photonics Res. **8**, 1676 (2020).
[62] X. Lu, A. Chanana, F. Zhou, M. Davanco, and K. Srinivasan, *Kerr optical parametric oscillation in a photonic crystal microring for accessing the infrared*, Opt. Lett. **47**, 3331 (2022).
[63] X. Lu, A. McClung, and K. Srinivasan, *High-Q slow light and its localization in a photonic crystal microring*, Nat. Photonics **16**, 66 (2022).
[64] Y. Liu, C. Lao, M. Wang, Y. Cheng, S. Fu, C. Gao, J. Wang, B.-B. Li, Q. Gong, Y.-F. Xiao *et al.*, *Integrated vortex soliton microcombs*, arXiv:2212.07639.

Correction: A minor error in Eq. (1) has been fixed. The previously published Fig. 3 contained an error in a label in panel (a) and has been replaced.